



1

2

3

4

5 **Abyssal plain hills and internal wave turbulence**

6

7

8

9

10

11 **by Hans van Haren¹**

12

13

14

15

16

17

18

19

20

21

22

23

24

25

26

27

28

29

30

31

32

¹Royal Netherlands Institute for Sea Research (NIOZ) and Utrecht University, P.O. Box 59,
1790 AB Den Burg, the Netherlands.

33

34

*e-mail: hans.van.haren@nioz.nl

35

36



37 **Abstract.**

38 A 400-m long array with 201 high-resolution NIOZ temperature sensors was
39 deployed above a northeast-equatorial Pacific hilly abyssal plain for 2.5 months. The
40 sensors sampled at 1 Hz, the lowest was at 7 m above the bottom ‘mab’. The aim was
41 to study internal waves and turbulent overturning away from large-scale ocean
42 topography. Topography consisted of moderate, a few 100 m elevated hills, providing
43 a mean bottom slope of one-third of that found at the Mid-Atlantic Ridge (on 2 km
44 horizontal scales). In contrast with observations over large-scale topography like
45 guyots, ridges and continental slopes, the present data showed a well-defined near-
46 homogeneous ‘bottom-boundary layer’ extending between <7 and 100 mab with a
47 maximum around 65 mab. The average thickness exceeded tidal current bottom-
48 frictional heights and internal wave breaking dominated over bottom friction. Near-
49 bottom fronts varied in time (and thus space). Occasional coupling was observed
50 between the interior internal waves breaking and the near-bottom overturning, with
51 varying up- and down- phase propagation. In contrast with currents that were dominated
52 by the semidiurnal tide, 200-m shear was dominant at (sub-)inertial frequencies. The
53 shear was so large that it provided a background of marginal stability for the straining
54 high-frequency internal wave field in the interior. Daily averaged turbulence dissipation
55 rate estimates were between 10^{-10} and $10^{-9} \text{ m}^2\text{s}^{-3}$, increasing with depth, while eddy
56 diffusivities were $O(10^{-4} \text{ m}^2\text{s}^{-1})$. This most intense ‘near-bottom’ internal wave-induced
57 turbulence will affect resuspension of sediments.

58

59



60 **1 Introduction**

61 The mechanical kinetic energy brought into the ocean via tides, atmospheric
62 disturbances and the Earth's rotation governs the motions in the density stratified ocean
63 interior. On the one hand isopycnals are set into oscillating motions as 'internal waves'.
64 On the other hand these oscillating motions deform nonlinearly and eventually
65 irreversibly lose their energy into turbulent mixing: Breaking internal waves are
66 suggested to be the dominant source of turbulence in the ocean (e.g., Eriksen, 1982;
67 Gregg, 1989; Thorpe, 2018). This turbulence is vital for life in the ocean, as it dominates
68 the diapycnal redistribution of components and suspended materials. It is also important
69 for the resuspension of bottom materials. Large-scale sloping ocean bottoms are
70 important for both the generation (e.g., Bell, 1975; LeBlond and Mysak, 1978;
71 Morozov, 1995) and the breaking of internal waves (e.g., Eriksen, 1982). Not only the
72 topography around ocean basin's edges act as source/sink of internal waves but
73 especially also the topography of ridges, mountain ranges and seamounts distributed
74 over the ocean floor. Above sufficiently steep slopes, exceeding those of the main
75 internal carrier (e.g. tidal) wave containing largest energy, and >1 km ($>$ the internal
76 wavelength) horizontal scale topography, turbulent mixing averages 10,000 times
77 molecular diffusion (e.g., Aucan et al., 2006; van Haren and Gostiaux, 2012). This
78 mixing is considered to be 'efficient' as the back and forth sloshing of the carrier wave
79 ensures a rapid restratification down to within a meter from the sea floor, while mixed
80 waters are transported into the interior along isopycnals. Sloping large-scale
81 topography has received more scientific interest than abyssal plains due to the higher
82 turbulence intensity of internal wave breaking. However, it may be questioned whether
83 the abyssal plain and its overlying waters may be called a 'quiescent zone'.



84 This is because occasional ‘benthic storms’ have been reported to disturb the
85 quiescence, even at great depths >5000 m (Hollister and McCave, 1984). The effects
86 can be great on sediment reworking and particles remain resuspended long after the
87 ‘storm’ has passed. Such resuspension has obvious effects on deep-sea benthic biology
88 and remineralization (e.g., Lochte, 1992). In order to avoid semantic problems, the term
89 ‘benthic boundary layer’ is reserved here for the sediment-water interface (at the bottom
90 of the water phase of the ocean), following common practice by sedimentologists and
91 marine chemists (e.g., Boudreau and Jørgensen, 2001). The term ‘bottom boundary
92 layer’ follows the physical oceanographic convention to describe the lower part of the
93 water phase of the ocean which is almost uniform in density, using the threshold
94 criterion of the large (100-m) scale buoyancy frequency $N < 3 \times 10^{-4} \text{ s}^{-1}$. This is the layer
95 of investigation here together with overlying more density stratified waters in the
96 interior. The amount of homogeneity is also a subject of study. Historic observations
97 have demonstrated the variability of the abyssal plain bottom boundary layer in space
98 and time (e.g., Wimbush, 1970; Armi and Millard, 1976; Armi and D’Asaro, 1980).

99 Similar to the ocean interior, waters above abyssal plains are considered calm ocean
100 regions in terms of weak turbulent exchange. However, the (bulk) Reynolds number Re
101 $= UL/\nu$ as a measure for the transition from laminar (‘molecular’) to turbulent flow is
102 not small. With the kinematic viscosity $\nu \approx 1.5 \times 10^{-6} \text{ m}^2 \text{ s}^{-1}$ to characterize the molecular
103 water properties and characteristic velocity, $U \approx 0.05 \text{ m s}^{-1}$, and length scale, $L \approx 30 \text{ m}$,
104 of the (internal wave) water flow, $Re \approx 10^6$, or highly turbulent (e.g., Tennekes and
105 Lumley, 1972; Fritts et al., 2016) even for the unbounded open ocean and atmosphere
106 interiors.

107 Both convective instability of gravitationally unstable denser over less dense water
108 and shear-induced Kelvin-Helmholtz instability (KH) are probable for internal wave



109 breaking, for a recent model see (Thorpe 2018). Earlier models (e.g., Garrett and Munk,
110 1972) suggested the latter were dominant, especially considering the construction of
111 the internal wave field of smallest vertical scales residing at the lowest frequencies (e.g.,
112 LeBlond and Mysak, 1978). Most kinetic energy is found at these frequencies and thus
113 a large background shear is generated (e.g., Alford and Gregg, 2001) through which
114 shorter length-scale waves near the buoyancy frequency propagate, break and overturn.
115 The result is an open ocean wave field that is highly intermittent producing a very
116 steppy, non-smooth sheet-and-layer-structured ocean interior stratification (e.g., Lazier,
117 1973; Fritts et al., 2016). In the near-surface ocean, such internal wave propagation and
118 deformation (straining) of stratification has been observed to migrate through the
119 density field in space and time.

120 The lower bound of inertio-gravity wave (IGW) frequencies is determined by the
121 local vertical Coriolis parameter, i.e. the inertial frequency, $f = 2\Omega\sin\phi$ of the Earth
122 rotational vector Ω at latitude ϕ . This bound becomes significantly modified to lower
123 sub-inertial frequencies under weak stratification ($\sim N^2$), when $N < 10f$, approximately.
124 From not-approximated equations, minimum and maximum IGW-frequencies are
125 calculated as $[\sigma_{\min}, \sigma_{\max}] = (s \mp (s^2 - f^2 N^2)^{1/2})^{1/2}$ using $2s = N^2 + f^2 + f_h^2 \cos^2 \gamma$, in which
126 γ is the angle to the north ($\gamma = 0$ denoting meridional propagation) and the horizontal
127 component of the Coriolis parameter $f_h = 2\Omega \cos \phi$ becomes important for internal wave
128 dynamics (e.g., LeBlond and Mysak, 1978; Gerkema et al., 2008).

129 In the present paper, detailed moored observations from a Pacific abyssal ‘plain’
130 confirm Lazier (1973)’s steppy sheet-and-layer stratification. The new observations are
131 used to investigate the interplay between motions in the stratified interior and the effects
132 on the bottom boundary layer. The small-scale topography may prove not negligible in
133 comparison with large oceanic ridges, seamounts and continental slopes: Following



134 Bell (1975), recent studies demonstrate the potential of substantial internal wave
135 generation by flow over abyssal hills under particular slope and stratification conditions
136 (e.g., Nikurashin et al., 2014; Hibiya et al., 2017). We are interested in observational
137 details of the IGW-induced turbulent processes.

138

139 **2 Data**

140 Observations were made from the German R/V Sonne above the abyssal hills in the
141 northeast-equatorial Pacific Ocean, West of the oriental Pacific Ridge (Fig. 1). The area
142 is not mountainous but also not flat. It is characterized by numerous hills, extending
143 several 100 m above the surrounding sea floor. The average bottom slope is $1.2\pm 0.6^\circ$,
144 computed from the lower panel of Fig. 1 using the 1'-resolution version of the Smith
145 and Sandwell (1997) seafloor topography. This slope is about three times larger than
146 that of the Hatteras plain (the area of observations by Armi and D'Asaro, 1980) and
147 about three times smaller than that for a similar size area from the Mid-Atlantic Ridge
148 (West of the Azores). SeaBird SBE911plus CTD profiles were collected 1 km around
149 $11^\circ 50.630'N$, $116^\circ 57.938' W$ in 4114 ± 20 m water depth at 20-23 March and 06 June
150 2015. Between 19 March and 02 June a taut-wire mooring was deployed at the above
151 coordinates. At this latitude, $f = 0.299\times 10^{-4} s^{-1}$ (≈ 0.4 cpd, cycles per day) and $f_h =$
152 $1.427\times 10^{-4} s^{-1}$ (≈ 2 cpd). A 130 m elevation has its ridge at approximately 5 km West
153 of the mooring.

154 The mooring consisted of 2700 N of net top-buoyancy at about 450 m from the
155 bottom. With current speeds of less than $0.15 m s^{-1}$, the buoy did not move more than
156 0.1 m vertically and 1 m horizontally, as was verified using pressure and tilt sensors.
157 The mooring line held three single point Nortek AquaDopp acoustic current meters, at
158 6, 207 and 408 mab, meters above the bottom. The middle current meter was clamped



159 to a 0.0063 m diameter plastic coated steel cable. To this 400 m long insulated cable
160 201 custom-made ‘NIOZ4’ temperature sensors were taped at 2.0 m intervals. To
161 deploy the 400 m long instrumented cable it was spooled from a custom-made large-
162 diameter drum with separate ‘lanes’ for T-sensors and the cable (Appendix A).

163 The NIOZ4 T-sensor noise level is <0.1 mK, the precision <0.5 mK (van Haren et
164 al., 2009; NIOZ4 is an update of NIOZ3 with similar characteristics). The sensors
165 sampled at a rate of 1 Hz and were synchronized via induction every 4 h, so that their
166 timing mismatch was <0.02 s and the 400 m profile was measured nearly
167 instantaneously. As in the abyssal area temperature variations are extremely small,
168 severe constraints were put on the de-spiking and noise levels of data. Under these
169 constraints, 35 (17% of) T-sensors showed electronic timing, calibration or noise
170 problems. Their data are no longer considered and are linearly interpolated. This low-
171 biases estimates of turbulence parameters like dissipation rate and diffusivity from T-
172 sensor data by about 10%. Appendix B describes further data processing details.

173 During three days around the time of mooring deployment and two days after
174 recovery, shipborne conductivity-temperature-depth (CTD) profiles were made for
175 monitoring the temperature-salinity variability from 5 m below the surface to 10 mab.
176 A calibrated SeaBird 911plus CTD was used. The CTD data were processed using the
177 standard procedures incorporated in the SBE-software, including corrections for cell
178 thermal mass using the parameter setting of Mensah et al. (2009) and sensor time-
179 alignment. All other analyses were performed with Conservative (~potential)
180 Temperature (Θ), absolute salinity SA and density anomalies σ_4 referenced to 4000
181 dbar using the GSW-software described in (IOC, SCOR, IAPSO, 2010).

182 After establishment of the temperature-density relationship (Appendix B), the
183 moored T-sensor data are used to estimate turbulence dissipation rate $\varepsilon = c_1^2 d^2 N^3$ and



184 vertical eddy diffusivity $K_z = m_1 c_1^2 d^2 N$ following the method of reordering potentially
185 unstable vertical density profiles in statically stable ones, as proposed by Thorpe
186 (1977). Here, d denotes the displacements between unordered (measured) and reordered
187 profiles. N denotes the buoyancy frequency computed from the reordered profiles. We
188 use standard constant values of $c_1 = 0.8$ for the Ozmidov/overturn scale factor and m_1
189 $= 0.2$ for the mixing efficiency (Osborn, 1980; Dillon, 1982; Oakey, 1982). The validity
190 of the latter is justified after inspection of the temperature-scalar spectral inertial
191 subrange content (cf. Section 3) and also considering the generally long averaging
192 periods over many (>1000) profiles. The buoyancy Reynolds number $Re_b = \epsilon/\nu N^2$ is
193 used to distinguish between areas of weak, $Re_b < 100$, and strong turbulence.

194 In the following, averaging over time is denoted by [...], averaging over depth-
195 range by $\langle \dots \rangle$. The specific averaging periods and ranges are indicated with the mean
196 values. The vertical coordinate z is taken upward from the bottom $z = 0$. Shear-induced
197 overturns are visually identified as inclined S-shapes in $\log(N)$ panels while convection
198 demonstrates more vertical columns (e.g., van Haren and Gostiaux, 2012; Fritts et al.,
199 2016). It is noted that both types occur simultaneously, as columns exhibit secondary
200 shear along the edges and KHi demonstrate convection in their interior core (Li and Li,
201 2004; Matsumoto and Hoshino, 2006).

202

203 **3 Observations**

204 High-resolution T-sensor data analysis was difficult because of the very small
205 temperature ranges and variations of only a few mK over, especially the lower, 100 m
206 of the observed range. This rate of variation is less than the local adiabatic lapse rate.
207 First, a spectral analysis is performed to investigate the internal wave and turbulence
208 ranges and slopes appearance. Then, particular turbulent overturning aspects of internal



209 wave breaking are demonstrated in magnifications of time-depth series. Finally,
210 profiles of mean turbulence parameter estimates are used to focus on the extent and
211 nature of the bottom boundary layer.

212 .

213 **3.1 Spectral overview**

214 The small temperature ranges are reflected in the low values of the large-scale
215 stratification (Fig. 2a). (Salinity contributes weakly to density variations, Appendix B).
216 Typical buoyancy periods are 3 h, increasing to roughly 9 h in near-homogeneous
217 layers, e.g., near the bottom. In spite of the weak stratification, the IGW-band,
218 approximately between and including f and N , is one order of magnitude wide. This
219 IGW-bandwidth is observable in spectra of turbulence dissipation rate (Fig. 2b) and
220 temperature variance (Fig. 2c).

221 The T-sensors have identical instrumental noise levels at frequencies $\sigma > 10^4$ cpd
222 and near-equal variance at sub-inertial frequencies $\sigma < f$ (Fig. 2c). In the frequency
223 range in between, and especially for $f \sim \sigma \sim N$, the upper T-sensor data demonstrate
224 largest variance by up to two orders of magnitude at $\sigma \approx N$ compared with the lower T-
225 sensor data. In this frequency range, the upper T-sensor spectrum has a slope of about
226 -1 (in the log-log domain), which reflects a dominance of smooth quasi-linear ocean-
227 interior IGW (van Haren and Gostiaux, 2009). Extending above this slope is a small
228 near-inertial peak reflecting rarely observed low internal wave frequency vertical
229 motions in weakly stratified waters (van Haren and Millot, 2005). The steep -3 roll-off
230 at super-buoyancy frequencies $\sigma > N$ is also associated with IGW. At frequencies in
231 between, and for the lower T-sensor data throughout the frequency range, a slope of -
232 $5/3$ is found. This reflects passive scalar turbulence dominated by shear (Tennekes and
233 Lumley, 1972). After sufficient averaging this passive scalar turbulence is efficient



234 (Mater et al., 2015). At intermediate depth levels, and in short frequency ranges of the
235 spectral data, slopes vary between -2 and -1. Slopes between $-5/3$ and -1 would point at
236 active scalar turbulence of convective mixing (Cimatoribus and van Haren, 2015) while
237 a slope of -2 reflects finestructure contamination (Phillips, 1971) or a saturated IGW-
238 field (Garrett and Munk, 1972).

239 While the upper T-sensor data contain most variance and hence most potential
240 energy in the IGW-band, the spectrum of estimated turbulence dissipation rate
241 demonstrates nearly two orders of magnitude higher variance for the lowest T-sensor
242 data around $\sigma \approx f$ (Fig. 2b). The stratification around the upper sensor supports
243 substantial internal waves, but weak turbulence provides a flat and featureless spectrum
244 of the dissipation rate time series. The lower layer ε -spectrum shows a relative peak
245 near $\sigma \approx 2f$, but no peaks at the inertial and semidiurnal tidal frequencies. The lack of
246 peaks at the latter frequencies is somewhat unexpected as the kinetic energy (Fig. 2b,
247 blue spectrum) is highly dominated by motions at M_2 and, to a lesser extent, at just
248 super-inertial $1.04f$.

249 In contrast, the ‘large-scale shear’ spectrum computed between current meters 20 m
250 apart (Fig. 2b, light-blue) shows a single dominant peak at just sub-inertial $0.99f$, with
251 a complete absence of a tidal peak. This reflects large quasi-barotropic vertical length
252 scales >400 m exceeding the mooring range at semidiurnal tidal frequencies and
253 commonly known ‘small’ ≤ 200 m vertical length scales at near-inertial frequencies.
254 The large-scale shear has an average magnitude of $\langle |\mathbf{S}| \rangle = 2 \times 10^{-4} \text{ s}^{-1}$ for 207-408 mab
255 and $1.6 \times 10^{-4} \text{ s}^{-1}$ for 6-207 mab, with peak values of $|\mathbf{S}| = 6 \times 10^{-4} \text{ s}^{-1}$ and $4 \times 10^{-4} \text{ s}^{-1}$,
256 respectively. Considering mean $\langle N \rangle \approx 5.5 \times 10^{-4} \text{ s}^{-1}$ with variations over one order of
257 magnitude, the mean gradient Richardson number $Ri = N^2/|\mathbf{S}|^2$ is just larger than unity
258 while marginally stable conditions ($Ri \approx 0.5$; Abarbanel et al., 1984) occur regularly.



259 Unfortunately, higher vertical resolution (acoustic profiler) current measurements were
260 not available to establish smaller scale shear variations associated with higher
261 frequency internal waves propagating through the (large-scale) shear generated by the
262 near-inertial motions. Such smaller-scale variations in shear are expected in association
263 with sheet-and-layer variation in stratification observed using the detailed high-
264 resolution T-sensors.

265

266 **3.2 Detailed periods**

267 The days shortly after deployment were amongst the quietest in terms of turbulence
268 during the entire mooring period. Nevertheless, some near-bottom and interior turbulent
269 overturning was observed occasionally (Fig. 3). For this example, averages of
270 turbulence parameters for one day time interval and 400 m vertical interval are
271 estimated as $[\langle \epsilon \rangle] = 1.2 \pm 0.8 \times 10^{-10} \text{ m}^2 \text{ s}^{-3}$ and $[\langle K_z \rangle] = 7 \pm 4 \times 10^{-5} \text{ m}^2 \text{ s}^{-1}$. These values
272 are typical for open-ocean ‘weak turbulence’ conditions although mean $Re_b \approx 200$.
273 Shortest isotherm distances are observed far (a few 100 m) above the bottom (Fig. 3a)
274 reflecting the generally stronger stratification (Fig. 3b) there. While the upper isotherms
275 smoothly oscillate with a periodicity close to the average buoyancy period of 3.2 h and
276 amplitudes of about 15 m, the stratification is organized in fine-scale layering
277 throughout, except for the lower 50 m of the range. Detailed inspection of sheets (large
278 values of small-scale N_s in Fig. 3b) demonstrates that they gain and lose strength ‘strain’
279 over time scales of the buoyancy period and shorter, that they merge and deviate, e.g.
280 around 300 mab between days 82.25 and 82.5 in Fig. 3b, also from the isotherms, in
281 association with the largest turbulent overturns (Fig. 3c) eroding them. This is reflected
282 in non-smooth isotherms, e.g., the interior overturning near 220 mab and day 82.6. The
283 patches of interior turbulent overturns, with displacements $|d| < 10 \text{ m}$ in this example,



284 are elongated in time-depth space, having timescales of up to the local buoyancy period
285 but not longer. Thus, it is unlikely they represent an intrusion that can have timescales
286 exceeding the local buoyancy timescale. Considering the 0.05 m s^{-1} average (tidal)
287 advection speed, their horizontal spatial extent is estimated to be about 500 m. This
288 extent is very close to the estimated baroclinic Rossby radius of deformation $Ro_i =$
289 $NH/n\pi f \approx 600 \text{ m}$ for vertical length scale $H = 100 \text{ m}$ and first mode $n = 1$.

290 The near-bottom range is different, with buoyancy periods approaching the
291 semidiurnal period, sometimes longer. However, a permanent turbulent and
292 homogeneous ‘bottom boundary layer’ is not observed, after further detailing (Fig. 4).

293 Examples of the upper, middle and lower 100 m of the T-sensor range are presented
294 in magnifications with different colour range, while maintaining the same isotherm
295 interval of 5 mK (Fig 4a-c). For this period, the mean flow is $0.04 \pm 0.01 \text{ m s}^{-1}$ towards
296 the SE, more or less off-slope of the small ridge located 5 km West of the mooring.
297 Between these panels, the high-frequency internal wave variations decrease in
298 frequency from upper to lower, but all panels do show overturning (e.g., around 330
299 mab and day 82.35 in Fig. 4a, 200 mab and day 82.6 in Fig. 4b and 35 mab and day
300 82.5 in Fig. 4c). In Fig. 4c the entire T-colour range represents only 1 mK. In this depth-
301 range, the low-frequency variation in temperature and, while not related, stratification
302 vary with a period of about 15.5 h. These variations do not have tidal periodicity and
303 are thus not reflecting bottom friction of the dominant tidal currents. Quasi-convective
304 overturning seems to occur after day 82.5. In the interior $> 100 \text{ mab}$ most overturning
305 seems shear-induced.

306 The overturning phenomena are more intensely observed during a less quiescent
307 day (Figs 5, 6), when turbulence values are about five times larger and mean $Re_b \approx$
308 1400. Between 300 and 400 mab isotherms remain quite smooth with near-linear



309 internal wave oscillations (Fig. 5a,b). The lower 300 m are quasi-permanently in
310 turbulent overturning but in specific bands only around about 310 mab and around 160
311 mab (Fig. 5c,d). Rms vertical overturn displacements are 2-3 times larger than in the
312 previous example. Their duration is commensurate the local buoyancy periods. The
313 smooth upper range isotherms centered around 360 mab are reflected in 75 m, one day
314 wide range of turbulence dissipation rates below threshold (Fig. 5d). But, above and
315 especially below, turbulent overturning is more intense, see also the detailed panels
316 (Fig. 6). While shear-induced overturning is seen, e.g. around 200 mab day 97.95 (Fig.
317 6b), convective turbulence columns are observed e.g. around 60 mab and day 98 (Fig.
318 6c).0. It is noted however, that in the presented data we cannot distinguish the fine-
319 detailed secondary overturning, e.g. shear-induced billow formation, on convection
320 'vertical columns'. In the lower 100 mab, overturning occurs on the large (~50 m,
321 hours) scales but also on much shorter time scales of 10 min. This results in isotherm
322 excursions that are faster than further away from the bottom. A coupling between
323 interior and near-bottom (turbulence and internal wave) motions is difficult to establish.
324 For example, short-scale (high-frequency $\sigma \gg f$) internal wave propagation >200 mab
325 shows downward phase (i.e., upward energy) propagation around day 97.75 (Fig. 5a)
326 with no clear correspondence with the lower 100 mab. Between days 98.2 and 98.5
327 however, the phase propagation appears upward (downward energy propagation), with
328 some indication for correspondence between upper 200-400 mab and lower 100 mab.
329 During this period the mean 0.04 m s^{-1} flow was towards W (upslope).

330 Another example of (two days) of rather intense turbulence is given in Figs 7,8,
331 with similar average values as in the previous example. It demonstrates in particular
332 relatively large-amplitude near-N internal waves (e.g., day 112.9, 310 mab) and bursts
333 of elongated weakly sloping (slanting) shear-induced overturning (e.g., day 113.2, 210



334 mab). The near- N waves appear quasi-solitary lasting for maximum 2 periods and
335 having about 30 m trough-crest level variation. As before, the vertical phase
336 propagation of these waves is ambiguous. In addition, very high-frequency ‘internal
337 waves’ around the small-scale buoyancy frequency are observed in the present
338 example, with small amplitudes <10 m visible in the isotherms around 300 mab, day
339 113.1.

340 The interior turbulent overturning appears more intense than in preceding examples,
341 with larger excursions of about $|50$ m] near 200 mab (Fig. 8b). This slanting layer of
342 elongated overturns seems originally shear-induced, but the overturns show clear
343 convective properties during the observed stage. The largest duration of patches is close
344 to the local mean buoyancy period. The entire layer demonstrates numerous shorter
345 time-scale overturning. Cross-overs (sudden changes in the vertical) are observed of
346 isotherms from thin high- N_s above low- N_s turbulent patches to below the low- N_s
347 patches, e.g. day 112.6 in Fig. 7b, and vice-versa, e.g. days 113.1 and 113.5 (recall that
348 small-scale N_s is computed from reordered Θ -profiles). This evidences one-sided,
349 rather than two-sided, turbulent mixing eroding a stratified layer either from below or
350 above.

351 The interior shear-induced turbulent overturning seems to have some
352 correspondence with the (top of) the near-bottom layer: on days 113.1-113.6 interior
353 mixing is accompanied by similar near-bottom mixing. The status of the near-bottom
354 layer ($z < 75$ mab) switches from large-scale convective instabilities (day < 113.1) to
355 stratified shear-induced overturning ($113.1 < \text{day} < 113.6$) and back to large-scale
356 convection with probably secondary shear instabilities (day > 113.6). This is visible in
357 the displacements (Fig. 7c) and dissipation rate (Fig. 7d), and part of it in detailed
358 temperature (Fig. 8c). The transitions between near-bottom ‘mixing regimes’ are



359 abruptly marked by near-bottom fronts. The mean 0.03 m s^{-1} flow is SW-directed (more
360 or less on-slope).

361 A two-day example of a relatively intensely turbulent near-bottom layer is given in
362 Figs 9,10. Two periods of about 9 h long (around days 135.9 and 136.8), 22 h apart,
363 demonstrate $>50 \text{ m}$ tall convective overturning extending nearly 100 mab. In between,
364 large-scale shear-induced overturning dominates, with a possible correspondence with
365 the interior in the form of a large-scale doming of isotherms and mixing in patches
366 around day 135.4 (lasting between $135.25 < \text{day} < 135.75$, generally around 200 mab).
367 The doming interior isotherms are not repeated in the lowermost isotherm capping of
368 the near-bottom layer, except perhaps for the down-going flank/front. The mean NE-
369 flow is 0.03 m s^{-1} (more or less off-slope). In this example as well as in previous ones
370 no evidence is found for ‘smooth’ intrusions, as demonstrated in the atmospheric DNS-
371 model by Fritts et al. (2016).

372

373 **3.3 Mean profiles**

374 The different mixing observed in the interior and near the bottom is reflected in the
375 ‘mean profiles’ of estimated turbulence parameters (Fig. 11a-c). These plots are
376 constructed from patching together consecutive one-day portions of data that are locally
377 drift-corrected. Time-average values of $[\epsilon]$, turbulent flux (providing average $[K_z]$) and
378 stratification (providing average $[N]$) are computed for each depth level. Averaging
379 over a day and longer is exceeding the buoyancy period even in these weakly stratified
380 waters. It is thus considered appropriate for internal wave induced mixing. This may
381 lead to some counter-intuitive averaging of displacement values greater than the local
382 distance to the bottom at particular depths. However, it is noted that Prandtl’s concept
383 of overturn sizes never exceeding the distance to a solid boundary was based on



384 turbulent friction of flow over a flat plate. As Tennekes and Lumley (1972) indicate,
385 such ‘mixing length theoretical concept’ may not be valid for flows with more than one
386 characteristic velocity. The present area is not known for geothermal fluxes, which are
387 also not observed in the present data. Here, the dominant turbulence generation process
388 seems induced by internal waves, as the observed turbulence well extends above the
389 layer $O(10\text{ m})$ of bottom friction.

390 The mean dissipation rate (Fig. 11a) and diffusivity (Fig. 11b) profiles are observed
391 to be largest between 7 and 60 mab, with values at least ten times higher than in the
392 interior. Near the bottom, stratification (Fig. 11c) is low but not as weak as some 15 m
393 higher-up. At about 30 mab local minima of $[\varepsilon]$ and $[K_z]$ are found. The average top of
394 weakly stratified $N < 3 \times 10^{-4} \text{ s}^{-1} \approx 4 \text{ cpd}$ ‘bottom boundary layer’ is at about 65 mab
395 (Fig. 11d). This sub-maximum in the pdf-distribution is broader than a second
396 maximum closer to the bottom, near 10 mab. This smaller bottom boundary layer is
397 probably induced by current friction, whereas the larger layer with an average of 65
398 mab probably by internal wave turbulence. Around 110 mab the maximum of the
399 bottom boundary layer is found with few occurrences (Fig. 11d). Around that height,
400 the profiles’ minimum turbulence values are observed at the depth of a weak local
401 maximum N (Fig. 11c). This layer separates the interior turbulent mixing with
402 maximum around 200 mab and the ‘near-bottom’ (<100 mab) mixing. From the
403 detailed data in Section 3.2 correspondence is observed between these layers, occurring
404 at least occasionally. Considering the weaker (mean) turbulence in between, it is
405 expected that the correspondence is communicated via internal waves and their shear.
406 As for freely propagating IGW, its frequency band has a one order of magnitude width
407 nearly everywhere, also close to the bottom (Fig. 11c). It is noted that inertial waves
408 from all (horizontal) angles can propagate through homogeneous, weakly and strongly



409 stratified layers, thus providing local shear (LeBlond and Mysak, 1978; van Haren and
410 Millot, 2004).

411

412 **4 Discussion**

413 The observed turbulence at 100 m and higher above the sea floor is mainly induced
414 by (sub-)inertial shear and (small-scale) internal wave breaking. This confirms
415 suggestions by Garrett and Munk (1972) for interior IGW. However, this shear is not
416 found to be decreasing with N (depth) in the present data. The >100 m depth range
417 is termed ‘the interior’ here although perhaps not being representative for the ‘mid-
418 water ocean’ as it is still within the height range of surrounding hilly topography. The
419 130 m high ridge 5 km West of the mooring is well outside the baroclinic Rossby radius
420 of deformation ($Ro_i \approx 500$ m). It unlikely influences the near-bottom turbulence here,
421 also because no correlation is found between across-slope flow and turbulence
422 intensity. The interior is occasionally found quiescent, with parameter values below the
423 threshold of very weak turbulence at about ten times molecular diffusion values. More
424 commonly the interior is found weakly-moderately turbulent with values
425 commensurate with open-ocean values (e.g., Gregg, 1989) following the interaction of
426 high-frequency internal waves breaking and inertial shear.

427 The observed dominance of near-inertial shear at the 200 m vertical scale, the
428 vertical separation distance between the current meters, is found far below the depths
429 of atmospheric disturbances generation near the surface. It seems related with local
430 generation, possibly in association with the hilly topography (St. Laurent et al., 2012;
431 Nikurashin et al., 2014; Alford et al., 2016; Hibiya et al., 2017). Also, the 200 m vertical
432 scale is observed to well exceed the excursion length (amplitude) of the internal waves,
433 the scale of overturn displacements and the size of most density stratification layering.



434 In contrast, above the Mid-Atlantic Ridge, where tidal currents are only twice as
435 energetic as near-inertial motions, the vertical length scale of tides equals that of near-
436 inertial motions around about 100-150 m (van Haren, 2007). There and in the open
437 ocean, near-inertial motions dominate shear at shorter scales with an expected peak
438 around 25 m (e.g., Gregg, 1989). As in the present data, the near-inertial shear showed
439 a shift to sub-inertial frequencies (van Haren, 2007). As the shear-magnitude was found
440 to be concentrated in sheets of high-N, it was suggested that this red-shift was due to
441 the broadening of the IGW-band in low-N layers. As a result, an effective coupling
442 between shear, stratification and the IGW-band was established. Considering the
443 similarity in sheet-and-layering and (large-scale) shear, such coupling is also suggested
444 in the present observations from the deep-sea over less dramatic topography.

445 As for a potential coupling between the interior and the more intense near-bottom
446 turbulence, internal wave propagation is observed in both up and down directions. In
447 the lower 50 mab the variability in turbulence intensity, in turbulence processes of shear
448 and convection, and in stratification demonstrates a non-smooth bottom boundary layer,
449 an active near-bottom turbulent zone ‘NBTZ’. As observed by Armi and D’Asaro
450 (1980), the extent above the bottom of turbulent mixing and a near-homogeneous mixed
451 layer varies between <7 and 100 mab with a mean of about 65 mab. This mean value
452 exceeds the common frictional boundary scales that can be computed for flow over flat
453 bottoms on a rotating sphere (Ekman, 1905), although parametrizations provide one
454 order of magnitude differences: $\delta = (2A/f)^{1/2}$, A the turbulent viscosity; if taken $A = K_z$
455 $\approx 10^{-4}$ - $10^{-3} \text{ m}^2 \text{ s}^{-1}$; Fig. 11b, $\delta \approx 2.5$ -8 m, or $\delta = 2 \times 10^{-3} U/f$; $U \approx 0.05 \text{ m s}^{-1}$: $\delta \approx 30 \text{ m}$
456 (e.g., Tennekes and Lumley, 1972). Both are (substantially) less than the NBTZ found
457 here, which thus seems to be governed by other processes such as IGW-breaking.



458 Sloping fronts are observed near the bottom in Armi and D'Asaro (1980)'s, Thorpe
459 (1983)'s and the present data. However, isopycnal transport of mixed waters seems not
460 away from the boundary as proposed in (Armi and D'Asaro, 1980) but rather into the
461 NBTZ sloping downward with time (present data). This governs the variable height of
462 the NBTZ.

463 Although bottom slopes were about three times larger in the Northeast Pacific than
464 above the Hatteras Plain, the present observations show many similarities as in Armi
465 and D'Asaro (1980). They also show many similarities with equivalent turbulence
466 estimates in both the interior and in the variable lower 100 mab compared with those
467 from above the central Alboran Sea, a basin of the Mediterranean Sea (van Haren,
468 2015), and with observations made in the southeast Pacific abyssal hill plains around -
469 07° 07.213' S, -088° 24.202' W, East of the oriental Pacific Ridge (unpublished results).
470 Thus it seems that the precise characteristics (slopes/heights) of the hilly topography is
471 not very relevant for the observed internal wave intensity and turbulence generation, as
472 long as the bottom is not a flat plate and the hills have IGW-scales. This probably holds
473 for both the present observations in the stratified interior and those in the NBTZ. The
474 tenfold larger turbulence intensity in the latter marks a relatively extended inertial
475 subrange. Although the near-bottom (6 mab) current magnitudes are typically 0.05 m
476 s⁻¹, up to about 0.10 m s⁻¹, the estimated turbulence intensity of 10³-10⁴ times larger
477 than molecular diffusion is sufficient to mix materials up to 100 mab, the extent of
478 observed vertical mixing in the layer adjacent of the bottom. This reflects previous
479 observations of nephels, turbid waters of enhanced suspended materials (Armi and
480 D'Asaro, 1980). It is expected that this material is resuspended locally, as the more
481 intensely turbulent steeper large-scale slopes are too far away horizontally, far beyond
482 the baroclinic Rossby radius of deformation.



483 For the future, modelling may provide better insights in the precise coupling
484 between near-inertial shear and internal wave breaking, leading to a combination of
485 convective and shear-induced overturning. The one-sided shear across thin-layer
486 stratification, as inferred from observed deviation of high-N sheets from isotherms and
487 associated with the vertical propagation direction of internal waves, may prove
488 important for the wave breaking.

489

490 **5 Conclusions**

491 From the present high-resolution temperature sensor data moored up to 400 m above
492 a hilly abyssal plain in the northeastern Pacific we find an interaction between small-
493 scale internal wave propagation, large-scale near-inertial shear and the near-bottom
494 water phase. In an environment where semidiurnal tidal currents dominate, 200-m shear
495 is largest at the inertial frequency and near-bottom turbulence dissipation rates are
496 largest at twice the inertial frequency. Due to internal wave propagation and occasional
497 breaking, stratification in the overlying waters is organized in thin sheets, with less
498 stratified waters in larger layers in between, but turbulent erosion occurs
499 asymmetrically. The average amount of turbulent overturns due to internal wave
500 breaking here and there is equal to open ocean turbulence, with intensities about 100
501 times those of molecular diffusion. The high-frequency internal waves propagate to
502 near the bottom and likely trigger ten times larger turbulence there as shown in time-
503 average vertical profiles. The result is a highly variable near-bottom turbulent zone,
504 which may be near-homogeneous over heights of less than 7 m and up to 100 m above
505 the bottom. This near-bottom turbulence is not predominantly governed by frictional
506 flows on a rotating sphere as in Ekman dynamics that occupy a shorter range $O(10\text{ m})$
507 above the bottom. Fronts occur and sudden isotherm-uplifts by solitary internal waves



508 as well. Turbulence seems shear dominated, but occurs in parallel with convection. The
509 shear is quasi-permanent because the dominant near-circular inertial motions have a
510 constant magnitude. It is expected that inertial shear dominates also on shorter scales
511 (not verifiable with the present current meter data), possibly added by smaller internal
512 wave shear. In the mean, turbulence dissipation rate exceeds the level of $10^{-11} \text{ m}^2\text{s}^{-3}$,
513 except for a 30 m thick layer around 100 mab.

514

515 *Acknowledgements.* I thank the master and crew of the R/V Sonne, J. Greinert and A.
516 Vink for their pleasant contributions to the overboard sea-operations. J. Blom
517 meticulously welded the thermistor string drums, including all of the pins. Financial
518 support came from the Netherlands Organization for the Advancement of Science
519 (N.W.O.), under grant number ALW-856.14.001 (JPIOceans).

520



521

APPENDIX A

522 **Thermistor string drum: A dedicated instrumented cable spool**

523 The deployment of a 1D T-sensors mooring, a thermistor string, is like most
524 commonly done for oceanographic moorings. Through the aft A-frame the top-buoy is
525 put first in the water whilst the ship is slowly steaming forward. The thermistor string
526 is coupled between buoy/other instrument(s) and other instrument(s)/acoustic releases
527 before attaching the weight that is dropped in free fall. The thermistor string is put
528 overboard through a wide, relatively large (0.4 m) diameter pulley, about 2 m above
529 deck, or, preferably, via a smoothly rounded gunwhale (Fig. A1). Up to 100 m length
530 of string holding typically 100 T-sensors can be put overboard manually by one or two
531 people. In that case, the string is laid on deck in neat long loops. The deployment of a
532 longer length string becomes more difficult, because of the weight and drag. For such
533 strings a 1.48 m inner diameter (1.60 m OD) 1400 pins drum is constructed to
534 safely and fully control their overboard operation (Fig. A1). The drum dimensions fit
535 in a sea container for easy transportation. The 0.04 m high metal pins guide the cables
536 and separate them from the T-sensors in ‘lanes’, while allowing the cables to switch
537 between lanes. The pins are screwed and welded in rows 0.027 and 0.023 m apart, the
538 former sufficiently wide to hold the sensors. Up to 18 T-sensors can be located in one
539 lane, before the next lane is filled. The drum has 14 double lanes and can store about
540 230 T-sensors and 450 m of cable in one layer. The longest string deployed successfully
541 thus far held 300 T-sensors and was 600 m long, with about one-quarter of the string
542 doubled on the drum. The doubling did not pose a problem, the sensors were thus well
543 separated that entanglement did not occur. For recovery, or deployment of strings
544 holding up to 150 T-sensors, a smooth surface drum is used of the same dimensions but
545 without pins.



546

APPENDIX B

547 **Temperature sensor data processing in weakly stratified waters**

548 High-resolution T-sensors can be used to estimate vertical turbulent exchange
549 across density-stratified waters, under particular constraints that are more difficult to
550 account for under weakly stratified conditions of $N < 0.1f$, say. As in the present data
551 the full temperature range is only 0.05°C over 400 m, careful calibration is needed to
552 resolve temperatures well below the 1-mK level, at least in relative precision.
553 Correction for instrumental electronic drift of 1-2 mK/mo requires shipborne high-
554 precision CTD knowledge of the local conditions and uses the physical condition of
555 static stability of the ocean at time scales longer than the buoyancy scale (longer than
556 the largest turbulent overturning timescale). CTD knowledge is also needed to use
557 temperature data as a tracer for density variations.

558 The NIOZ4 T-sensor noise level is nominally $<1 \times 10^{-4}^{\circ}\text{C}$ (van Haren et al., 2009;
559 NIOZ4 is an update of NIOZ3 with similar characteristics) and thus potentially of
560 sufficient precision. A custom-made laboratory tank can hold up to 200 T-sensors for
561 calibration against an SBE35 Deep Ocean Standards high precision platinum
562 thermometer to an accuracy of $2 \times 10^{-4}^{\circ}\text{C}$ over ranges of about 25°C in the domain of [-
563 4, $+35^{\circ}\text{C}$]. Due to drift in the NTC-resistor and other electronics of the T-sensors, such
564 accuracy can be maintained for a period of about four weeks after aging. However, this
565 period is generally shorter than the mooring period (of up to 1.5 years). During post-
566 processing, sensor-drifts are corrected by subtracting constant deviations from a smooth
567 profile over the entire vertical range and averaged over typical periods of 4-7 days.
568 Such averaging periods need to be at least longer than the buoyancy period to guarantee
569 that the water column is stably stratified by definition (in the absence of geothermal
570 heating as in the present area). Conservatively, they are generally taken longer than the



571 inertial period (here: 2.5 days). In weakly stratified waters as the present observations,
572 the effect of drift is relatively so large that the smooth polynomial is additionally forced
573 to the smoothed CTD-profile obtained during the overlapping time-period of data
574 collection (Fig. B1). In the present case, this can only be done during the first few days
575 of deployment and corrections for drift during other periods are made by adapting the
576 local smooth polynomial with the difference of the (smooth-average) CTD-profile and
577 the smooth polynomial of the first few days of deployment.

578 The calibrated and drift-corrected T-sensor data are transferred to Conservative
579 (\sim potential) Temperature (Θ) values (IOC, SCOR, IAPSO, 2010), before they are used
580 as a tracer for potential density variations $\delta\sigma_4$, referenced to 4000 dbar, following the
581 constant linear relationship obtained from best-fit data using all nearby CTD-profiles
582 over the mooring period and across the lower 400 m (Fig. B2). As temperature
583 dominates density variations, this relationship's slope or apparent thermal expansion
584 coefficient is $\alpha = \delta\sigma_4/\delta\Theta = -0.223 \pm 0.005 \text{ kg m}^{-3} \text{ }^\circ\text{C}^{-1}$ (n=5). The resolvable turbulence
585 dissipation rate threshold averaged over a 100-m vertical range is approximately 3×10^7
586 $\text{m}^2 \text{ s}^{-3}$.

587



588 **References**

- 589 Abarbanel, H. D. I., Holm, D. D., Marsden, J.E., and Ratiu, T.: Richardson number
590 criterion for the nonlinear stability of three-dimensional stratified flow, *Phys. Rev.*
591 *Lett.*, 52, 2352-2355, 1984.
- 592 Alford, M. H. and Gregg, M. C.: Near-inertial mixing: Modulation of shear, strain and
593 microstructure at low latitude, *J. Geophys. Res.*, 106, 16,947-16,968, 2001.
- 594 Alford, M. H., MacKinnon, J. A., Simmons, H. L., and Nash, J. D.: Near-inertial
595 internal gravity waves in the ocean, *Ann. Rev. Mar. Sci.*, 8, 95-123, 2017.
- 596 Armi, L. and E. D'Asaro, E.: Flow structures of the benthic ocean, *J. Geophys. Res.*,
597 85, 469-483, 1980.
- 598 Armi, L. and Millard, R. C.: The bottom boundary layer of the deep ocean. *J. Geophys.*
599 *Res.*, 81, 4983-4990, 1976.
- 600 Aucan, J., Merrifield, M. A., Luther, D. S., and Flament, P.: Tidal mixing events on the
601 deep flanks of Kaena Ridge, Hawaii, *J. Phys. Oceanogr.*, 36, 1202-1219, 2006.
- 602 Bell, T. H.: Topographically generated internal waves in the open ocean, *J. Geophys.*
603 *Res.*, 80, 320-327, 1975.
- 604 Boudreau, B. P. and Jørgensen, B. B. (eds): *The benthic boundary layer: Transport*
605 *processes and biogeochemistry*, Oxford University Press, 2001.
- 606 Cimattoribus, A. A. and van Haren, H.: Temperature statistics above a deep-ocean
607 sloping boundary, *J. Fluid Mech.*, 775, 415-435, 2015.
- 608 Dillon, T. M.: Vertical overturns: A comparison of Thorpe and Ozmidov length scales,
609 *J. Geophys. Res.*, 87, 9601-9613, 1982.
- 610 Ekman, V. W.: On the influence of the Earth's rotation on ocean-currents, *Ark. Math.*
611 *Astron. Fys.*, 2(11), 1-52, 1905.



- 612 Eriksen, C. C.: Observations of internal wave reflection off sloping bottoms, J.
613 Geophys. Res., 87, 525-538, 1982.
- 614 Fritts, D. C., Wang, L., Geller, M. A., Lawrence, D. A., Werne, J., and Balsley, B. B.:
615 Numerical modeling of multiscale dynamics at a high Reynolds number:
616 Instabilities, turbulence, and an assessment of Ozmidov and Thorpe scales, J.
617 Atmos. Sci., 73, 555-578, 2016.
- 618 Gerkema, T., Zimmerman, J. T. F., Maas, L. R. M., and van Haren, H.: Geophysical
619 and astrophysical fluid dynamics beyond the traditional approximation, Rev.
620 Geophys., 46, RG2004, doi:10.1029/2006RG000220, 2008.
- 621 Garrett, C. and Munk, W.: Oceanic mixing by breaking internal waves, Deep-Sea Res.,
622 19, 823-832, 1972.
- 623 Gregg, M. C.: Scaling turbulent dissipation in the thermocline, J. Geophys. Res., 94,
624 9686-9698, 1989.
- 625 Hibiya, T., Ijichi, T., and Robertson, R.: The impacts of ocean bottom roughness and
626 tidal flow amplitude on abyssal mixing, J. Geophys. Res., 122, 5645-5651,
627 doi:10.1002/2016JC012564, 2017.
- 628 Hollister, C. D. and McCave, I. N.: Sedimentation under deep-sea storms, Nature, 309,
629 220-225, 1984.
- 630 IOC, SCOR, IAPSO: The international thermodynamic equation of seawater – 2010:
631 Calculation and use of thermodynamic properties, Intergovernmental
632 Oceanographic Commission, Manuals and Guides No. 56, UNESCO, Paris, France,
633 2010.
- 634 Lazier, J. R. N.: Temporal changes in some fresh water temperature structures, J. Phys.
635 Oceanogr., 3, 226-229, 1973.
- 636 LeBlond, P. H. and Mysak, L. A.: Waves in the Ocean, Elsevier, New York, 1978.



- 637 Li, S. and Li, H.: Parallel AMR code for compressible MHD and HD equations, T-7,
638 MS B284, Theoretical division, Los Alamos National Laboratory,
639 <http://math.lanl.gov/Research/Highlights/amrmhd.shtml>, 2006.
- 640 Lochte, K.: Bacterial Standing Stock and Consumption of Organic Carbon in the
641 Benthic Boundary Layer of the Abyssal North Atlantic, In: Rowe, G. T. and
642 Pariente, V. (eds), Deep-Sea Food Chains and the Global Carbon Cycle, Kluwer,
643 Dordrecht, 1-10, 1992.
- 644 Mater, B. D., Venayagamoorthy, S. K., St. Laurent, L., and Moum, J. N.: Biases in
645 Thorpe scale estimates of turbulence dissipation. Part I: Assessments from large-
646 scale overturns in oceanographic data, *J. Phys. Oceanogr.*, 45, 2497-2521, 2015.
- 647 Matsumoto, Y. and Hoshino, M.: Onset of turbulence by a Kelvin-Helmholtz vortex,
648 *Geophys. Res. Lett.*, 31, L02807, doi:10.1029/2003GL018195, 2004.
- 649 Mensah, V., Le Menn, M., and Morel, Y.: Thermal mass correction for the evaluation
650 of salinity, *J. Atmos. Ocean. Tech.*, 26, 665-672, 2009.
- 651 Morozov, E. G.: Semidiurnal internal wave global field, *Deep-Sea Res. I*, 42, 135-148,
652 1995.
- 653 Nikurashin, M., Ferrari, R., Grisouard, N., and K. Polzin, K.: The impact of finite-
654 amplitude bottom topography on internal wave generation in the southern ocean, *J.*
655 *Phys. Oceanogr.*, 44, 2938-2950, 2014.
- 656 Oakey, N. S.: Determination of the rate of dissipation of turbulent energy from
657 simultaneous temperature and velocity shear microstructure measurements, *J. Phys.*
658 *Oceanogr.*, 12, 256-271, 1982.
- 659 Osborn, T. R.: Estimates of the local rate of vertical diffusion from dissipation
660 measurements, *J. Phys. Oceanogr.*, 10, 83-89, 1980.



- 661 Phillips, O. M.: On spectra measured in an undulating layered medium, *J. Phys.*
662 *Oceanogr.*, 1, 1-6, 1971.
- 663 Smith, W. H. F. and Sandwell, D. T.: Global seafloor topography from satellite
664 altimetry and ship depth soundings, *Science*, 277, 1957-1962, 1997.
- 665 St. Laurent, L. C., Garabato, A. C. N., Ledwell, J. R., Thurnherr, A. M., Toole, J. M.,
666 and Watson, A. J.: Turbulence and diapycnal mixing in Drake Passage, *J. Phys.*
667 *Oceanogr.*, 42, 2143-2152, 2012
- 668 Tennekes, H. and Lumley, J. L.: A first course in Turbulence, MIT Press, Cambridge,
669 1972.
- 670 Thorpe, S. A.: Turbulence and mixing in a Scottish loch, *Phil. Trans. Roy. Soc. Lond.*
671 A, 286, 125-181, 1977.
- 672 Thorpe, S. A.: Benthic observations on the Madeira abyssal plain: *Fronts, J. Phys.*
673 *Oceanogr.*, 13, 1430-1440, 1983.
- 674 Thorpe, S. A.: Models of energy loss from internal waves breaking in the ocean, *J. Fluid*
675 *Mech.*, 836, 72-116, 2018.
- 676 van Haren, H.: Inertial and tidal shear variability above Reykjanes Ridge, *Deep-Sea.*
677 *Res. I*, 54, 856-870, 2007.
- 678 van Haren, H.: Impressions of the turbulence variability in a weakly stratified, flat-
679 bottom deep-sea ‘boundary layer’, *Dyn. Atmos. Oceans*, 69, 12-25, 2015.
- 680 van Haren, H. and L. Gostiaux, L.: High-resolution open-ocean temperature spectra, *J.*
681 *Geophys. Res.*, 114, C05005, doi:10.1029/2008JC004967, 2009.
- 682 van Haren, H. and Gostiaux, L.: Detailed internal wave mixing above a deep-ocean
683 slope, *J. Mar. Res.*, 70, 173-197, 2012.
- 684 van Haren, H. and Millot, C.: Rectilinear and circular inertial motions in the Western
685 Mediterranean Sea, *Deep-Sea Res. I*, 51, 1441-1455, 2004.



686 van Haren, H. and Millot, C.: Gyroscopic waves in the Mediterranean Sea, *Geophys.*

687 *Res. Lett.*, 32, L24614, doi:10.1029/2005GL023915, 2005.

688 van Haren, H., Laan, M., Buijsman, D.-J., Gostiaux, L., Smit, M. G., and Keijzer, E.:

689 NIOZ3: independent temperature sensors sampling yearlong data at a rate of 1 Hz,

690 *IEEE J. Ocean. Eng.*, 34, 315-322, 2009.

691 Wimbush, M.: Temperature gradient above the deep-sea floor, *Nature*, 227, 1041-1043,

692 1970.

693



694 **Figure 1.** Bathymetry map of the tropical Northeast Pacific based on the 9.1 ETOPO-
695 1 version of satellite altimetry-derived data by Smith and Sandwell (1997). The
696 black dot in the lower panel indicates mooring and CTD positions. Note the different
697 colour ranges between the panels.

698

699 **Figure 2.** Stratification and spectral overview. **(a)** Vertical profiles of buoyancy
700 frequency scaled with the local horizontal component of the Coriolis parameter f_h
701 and smoothed over 50 dbar (~50 m), from all five CTD-stations to within 1 km from
702 the mooring. The blue, green and red profiles are made around the time of mooring
703 deployment. **(b)** Weakly smoothed (10 degrees of freedom, dof) spectra of kinetic
704 energy (upper current meter; green) and current difference (between upper and
705 middle current meters; light-blue). In red and purple the spectra of 150 s sub-
706 sampled time series of 100 m vertically averaged turbulence dissipation rates for
707 lower (7-107 m above the bottom, mab) and upper (307-407 mab) T-sensor data
708 segments, respectively. The inertial frequency f , f_h including several higher
709 harmonics, buoyancy frequency N incl. range, and the semidiurnal lunar tidal
710 frequency M_2 are indicated. N_{\max} indicates the maximum small-scale buoyancy
711 frequency. **(c)** Weakly smoothed (10 dof) spectra of 2 s sub-sampled temperature
712 data from 3 depths representing upper, middle and lower levels. For reference,
713 several slopes with frequency are indicated.

714

715 **Figure 3.** One day sample detail of moored temperature observations during relatively
716 calm conditions (on the day of calibration in the beginning of the record). **(a)**
717 Conservative Temperature. The black contour lines are drawn every 0.005°C. At
718 the top from left to right, two time references indicate the mean (purple bar) and



719 shortest (green bar) buoyancy periods found in this data-detail. Values for time-
720 depth-range-mean parameters are given of buoyancy Reynolds number (light-blue),
721 buoyancy frequency (blue), turbulence dissipation rate (red) and turbulent eddy
722 diffusivity (black). Errors for the latter two are to within a factor of 2,
723 approximately. **(b)** Logarithm of small-scale (2 dbar) buoyancy frequency from
724 reordered temperature profiles. The black isotherms are reproduced from panel a.
725 **(c)** Thorpe displacements between raw-(panel a.) and reordered T-profiles. **(d)**
726 Logarithm of turbulence dissipation rate.

727

728 **Figure 4.** Magnifications of Fig. 3a using different colour ranges but maintaining the 5
729 mK distance between isotherms. **(a)** Upper 100 m. **(b)** Approximately middle 100
730 m. **(c)** Bottom 100 m; note the entire colour range extending over 1 mK only. **(d)**
731 Time series of logarithm of vertical-mean turbulence dissipation rates from Fig. 3d
732 for the panels a,b,c labelled u,m,b, respectively.

733

734 **Figure 5.** As Fig. 3 with identical colour ranges, but for a one-day period with more
735 intense turbulence especially near the bottom.

736

737 **Figure 6.** As Fig. 4, but associated with Fig. 5 and using different colour ranges.

738

739 **Figure 7.** As Fig. 3 with identical colour ranges, but for a two-day period with
740 occasional long shear turbulence.

741

742 **Figure 8.** As Fig. 4, but associated with Fig. 7 and using different colour ranges.

743



744 **Figure 9.** As Fig. 3 with identical colour ranges, but for a two-day period with some
745 intense convective turbulence also near the bottom.

746

747 **Figure 10.** As Fig. 4, but associated with Fig. 9 and using different colour ranges.

748

749 **Figure 11.** Profiles of turbulence parameters from entire-record time-averaged
750 estimates using 1-day drift-corrected, 150 s sub-sampled moored temperature data.

751 (a) Logarithm of dissipation rate. (b) Logarithm of eddy diffusivity. (c) Logarithm

752 of small-scale (2 dbar) buoyancy frequency from the T-sensors (black) with for

753 comparison the mean of the five CTD-profiles smoothed over 50 dbar vertical

754 intervals from Fig. 2a (red). The green dashed curves indicate the minimum (to the

755 left of the f-line) and maximum (to the right of the N-profile) inertio-gravity wave

756 bounds for meridional internal wave propagation (see text). (d) Pdf of the ‘bottom

757 boundary layer height’, the level of the first passage of threshold $N > 3 \times 10^{-4} \text{ s}^{-1}$

758 indicating the stratification capping the ‘near-homogeneous’ layer from the bottom

759 upward. Two peaks are visible, one near 10 mab attributable to bottom friction,

760 another around 65 mab attributable to internal wave-induced turbulence.

761

762 **Fig. A1.** Photo of thermistor string deployment using the instrumented cable spooling

763 drum onboard R/V Sonne.

764

765 **Fig. B1.** Conservative Temperature profiles with depth over the lower 400 mab. One-

766 day mean moored sensor data, raw data after calibration (thin black line, yellow-

767 filled) and smooth high-order polynomial fit (thick black solid line). In red are three

768 CTD-profiles within 1 km from the mooring during the first days of deployment



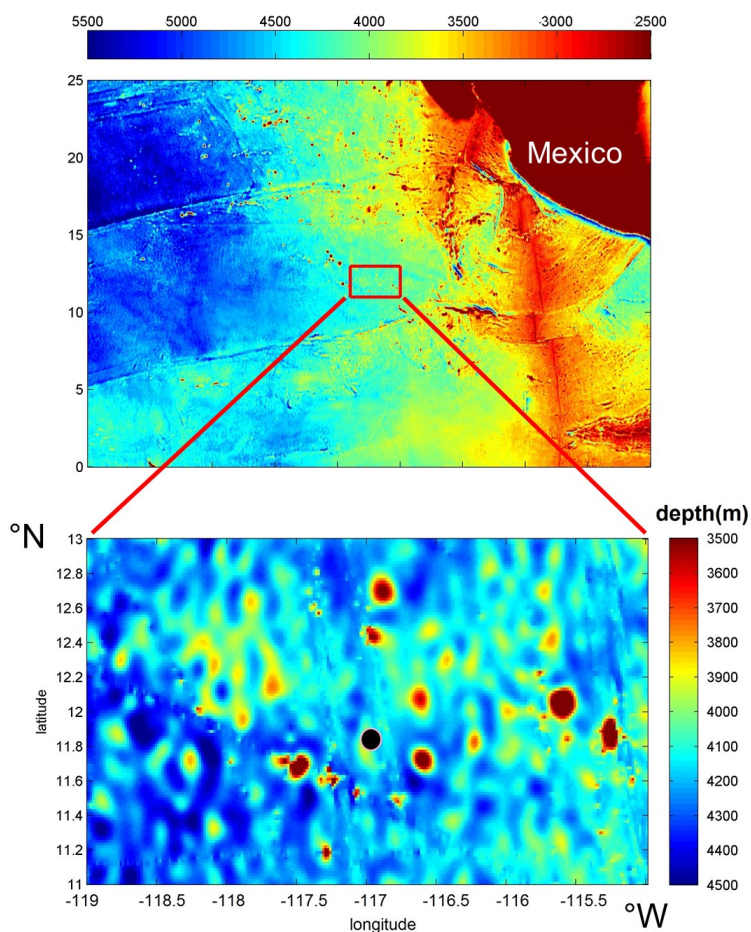
769 (two solid profiles on day 80/81 coincide in time with moored data mean), in blue-
770 dashed are two CTD-profiles after recovery of the mooring. The mean of the two
771 solid red profiles is given by the red/dash-dot profile, 0.015 °C off-set for clarity,
772 with its smooth high-order polynomial fit in light-blue to which the moored data are
773 corrected.

774

775 **Fig. B2.** Lower 400 m of five CTD-profiles obtained near the T-sensor mooring. Red
776 data are from around the beginning of the moored period, blue from after recovery.
777 (a) Conservative Temperature. (b) Absolute Salinity with x-axis range matching the
778 one in a. in terms of equivalent relative contributions to density variations. The noise
779 level is larger than for temperature. (c) Density anomaly referenced to 4000 dbar.
780 (d) Density anomaly – Conservative Temperature relationship ($\delta\sigma_4 = \alpha\delta\Theta$). The
781 data yielding two representative slopes after linear fit are indicated (the mean of 5
782 profiles gives $\langle\alpha\rangle = -0.223\pm 0.005 \text{ kg m}^{-3} \text{ }^\circ\text{C}^{-1}$).

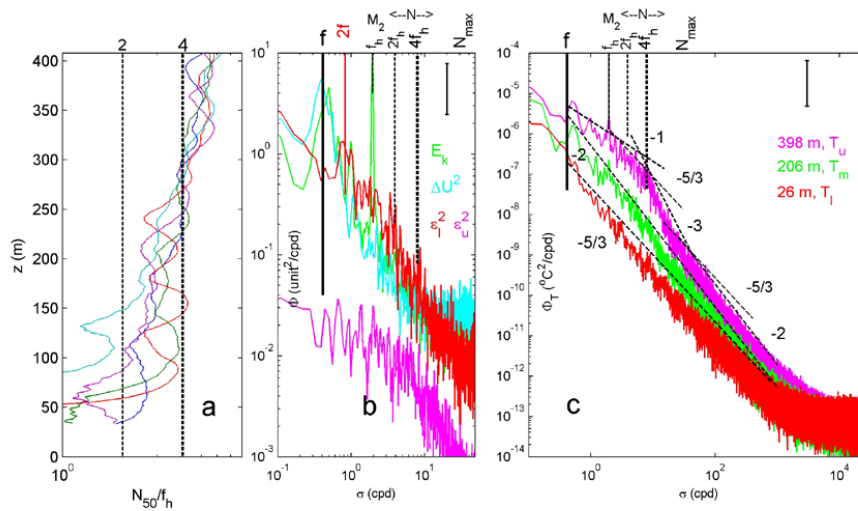
783

784



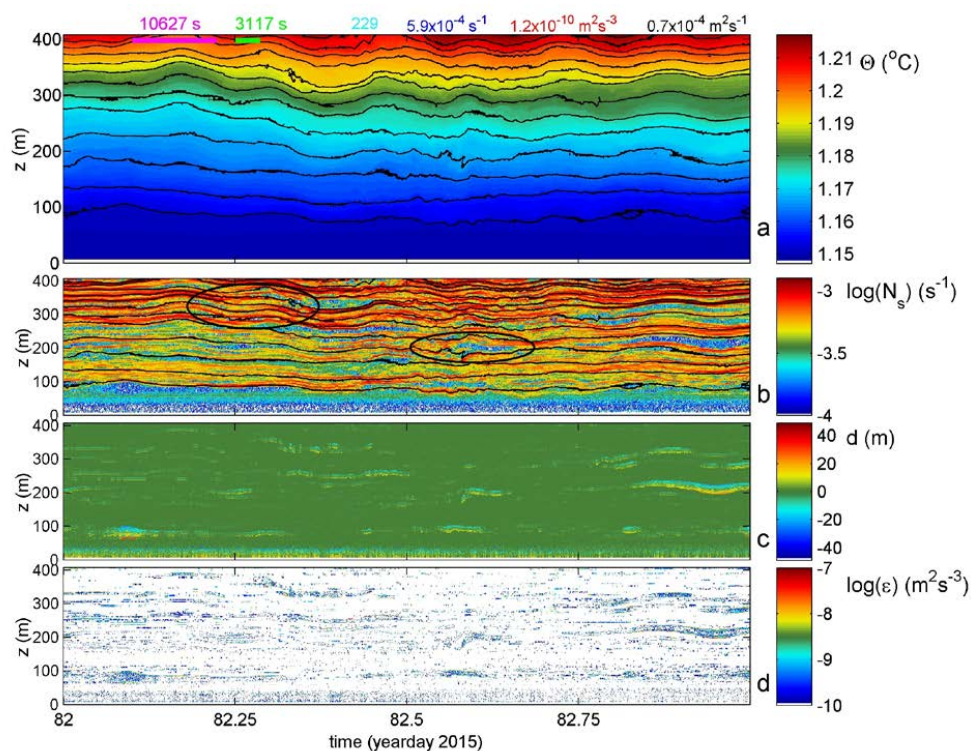
785
786
787
788
789
790

Figure 1. Bathymetry map of the tropical Northeast Pacific based on the 9.1 ETOPO-1 version of satellite altimetry-derived data by Smith and Sandwell (1997). The black dot in the lower panel indicates mooring and CTD positions. Note the different colour ranges between the panels.



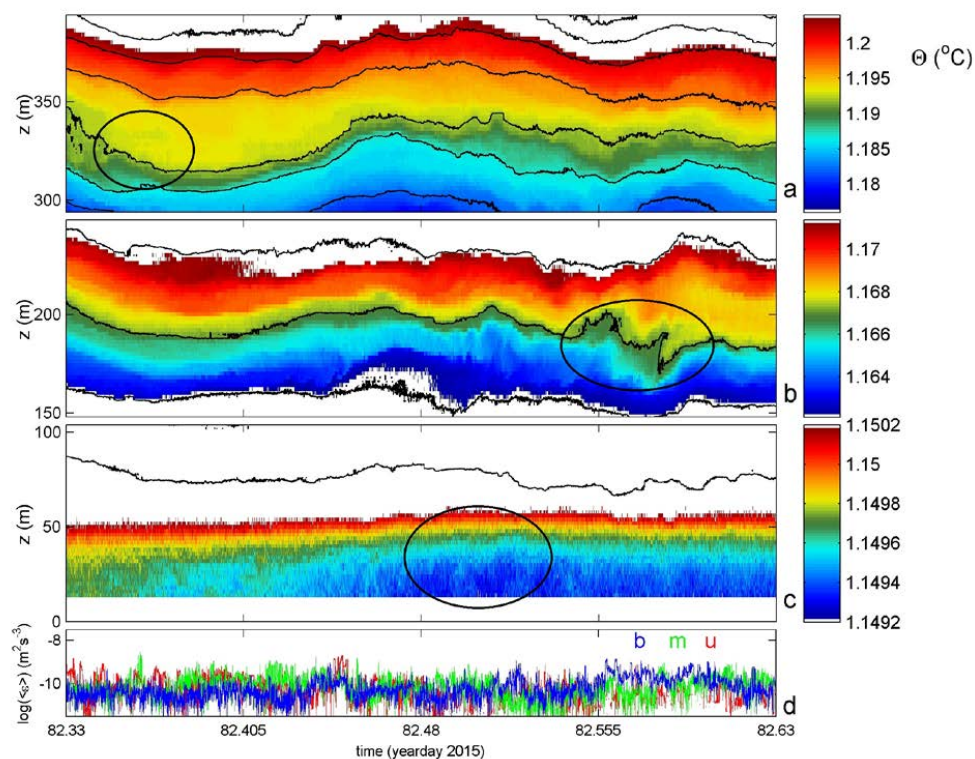
791
 792
 793
 794
 795
 796
 797
 798
 799
 800
 801
 802
 803
 804
 805
 806
 807

Figure 2. Stratification and spectral overview. (a) Vertical profiles of buoyancy frequency scaled with the local horizontal component of the Coriolis parameter f_h and smoothed over 50 dbar (~50 m), from all five CTD-stations to within 1 km from the mooring. The blue, green and red profiles are made around the time of mooring deployment. (b) Weakly smoothed (10 degrees of freedom, dof) spectra of kinetic energy (upper current meter; green) and current difference (between upper and middle current meters; light-blue). In red and purple the spectra of 150 s sub-sampled time series of 100 m vertically averaged turbulence dissipation rates for lower (7-107 m above the bottom, mab) and upper (307-407 mab) T-sensor data segments, respectively. The inertial frequency f , f_h including several higher harmonics, buoyancy frequency N incl. range, and the semidiurnal lunar tidal frequency M_2 are indicated. N_{max} indicates the maximum small-scale buoyancy frequency. (c) Weakly smoothed (10 dof) spectra of 2 s sub-sampled temperature data from 3 depths representing upper, middle and lower levels. For reference, several slopes with frequency are indicated.



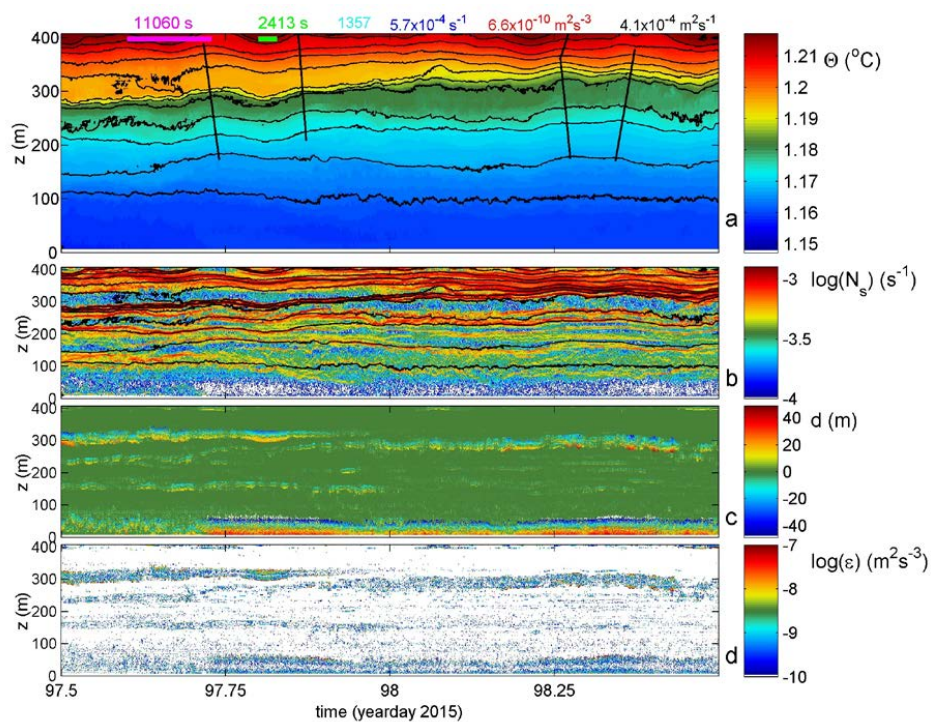
808
 809
 810
 811
 812
 813
 814
 815
 816
 817
 818
 819
 820
 821

Figure 3. One day sample detail of moored temperature observations during relatively calm conditions (on the day of calibration in the beginning of the record). (a) Conservative Temperature. The black contour lines are drawn every 0.005°C . At the top from left to right, two time references indicate the mean (purple bar) and shortest (green bar) buoyancy periods found in this data-detail. Values for time-depth-range-mean parameters are given of buoyancy Reynolds number (light-blue), buoyancy frequency (blue), turbulence dissipation rate (red) and turbulent eddy diffusivity (black). Errors for the latter two are to within a factor of 2, approximately. (b) Logarithm of small-scale (2 dbar) buoyancy frequency from reordered temperature profiles. The black isotherms are reproduced from panel a. (c) Thorpe displacements between raw-(panel a.) and reordered T-profiles. (d) Logarithm of turbulence dissipation rate.



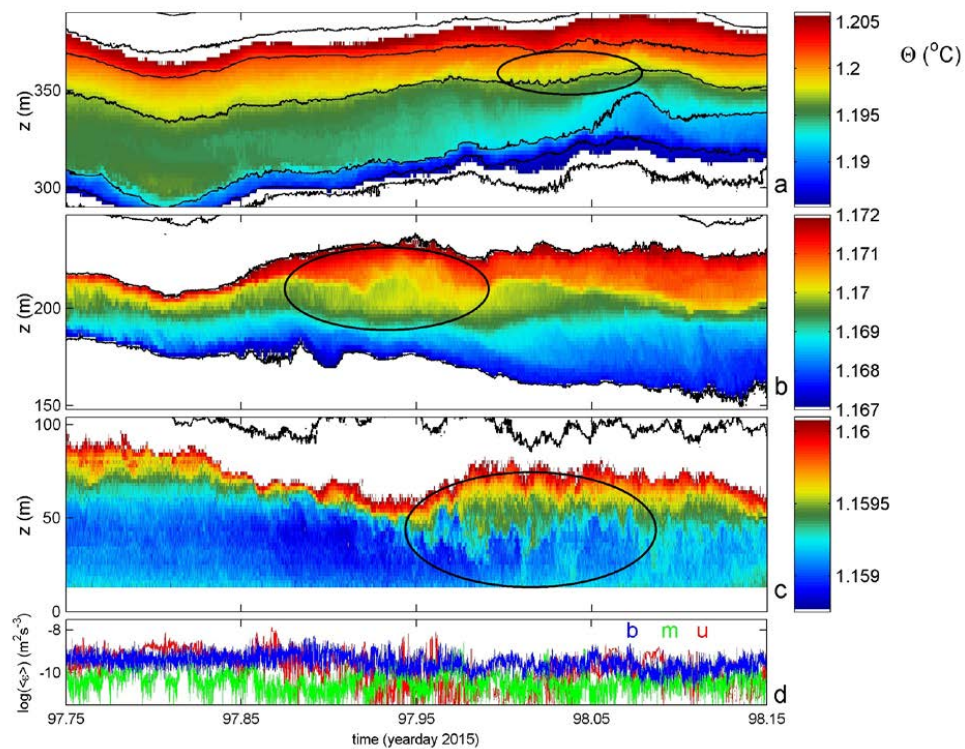
822
823
824
825
826
827
828

Figure 4. Magnifications of Fig. 3a using different colour ranges but maintaining the 5 mK distance between isotherms. (a) Upper 100 m. (b) Approximately middle 100 m. (c) Bottom 100 m; note the entire colour range extending over 1 mK only. (d) Time series of logarithm of vertical-mean turbulence dissipation rates from Fig. 3d for the panels a,b,c labelled u,m,b, respectively.



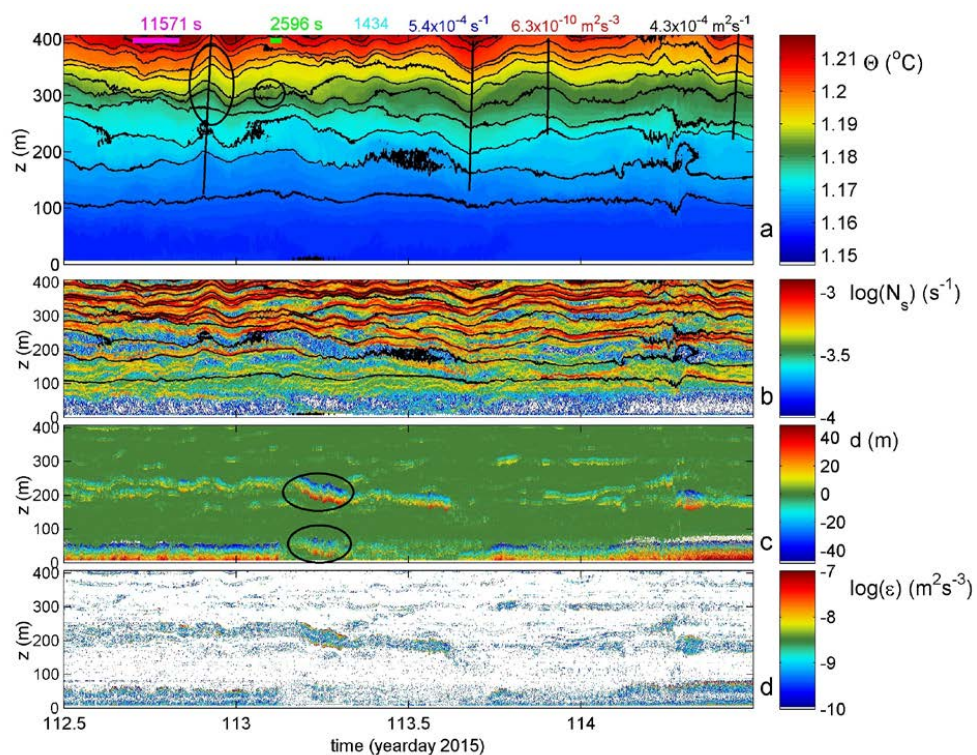
829
830
831
832

Figure 5. As Fig. 3 with identical colour ranges, but for a one-day period with more intense turbulence especially near the bottom.



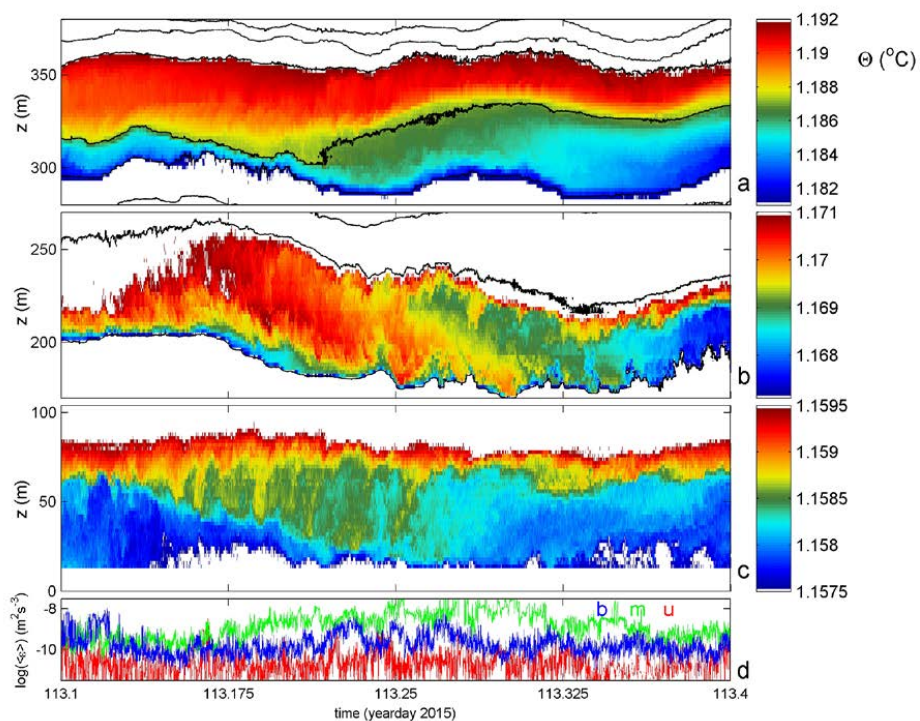
833
834
835

Figure 6. As Fig. 4, but associated with Fig. 5 and using different colour ranges.



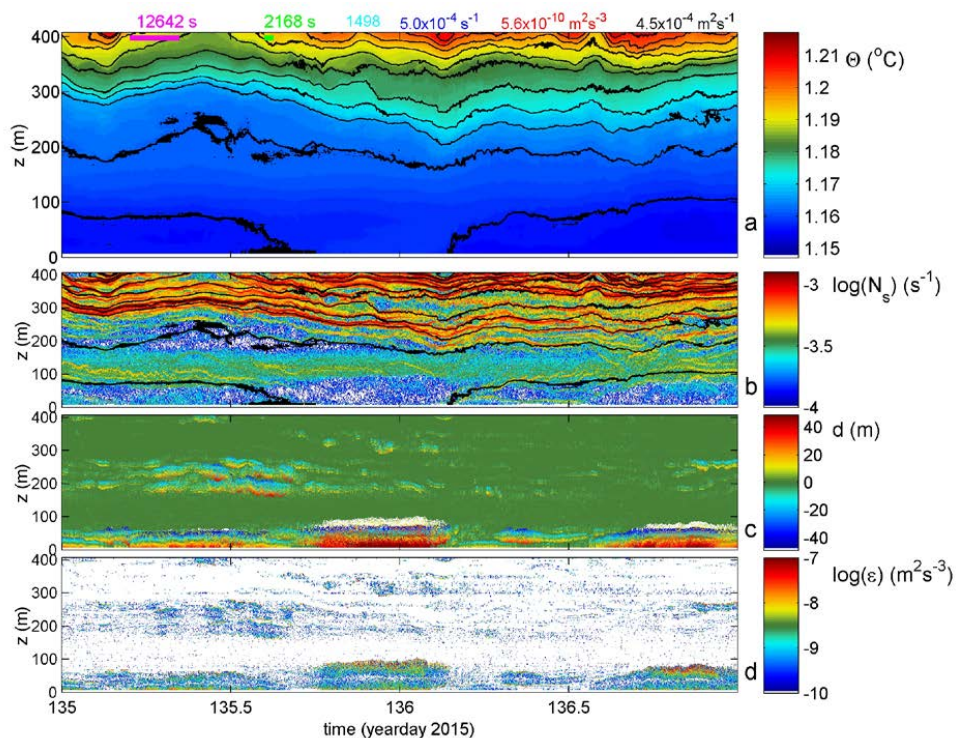
836
837
838
839

Figure 7. As Fig. 3 with identical colour ranges, but for a two-day period with occasional long shear turbulence.



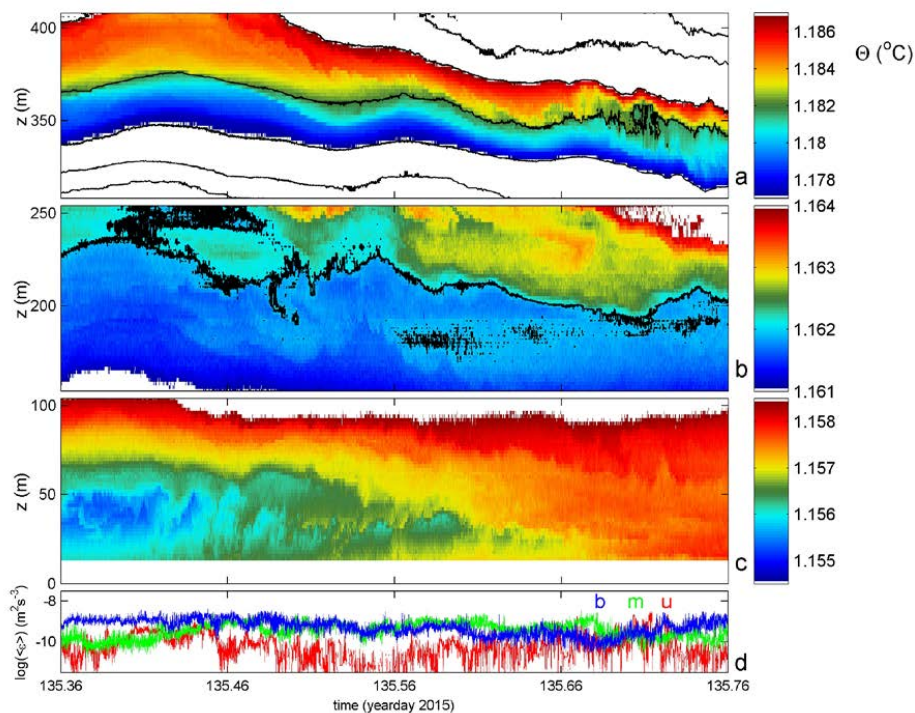
840
841
842

Figure 8. As Fig. 4, but associated with Fig. 7 and using different colour ranges.



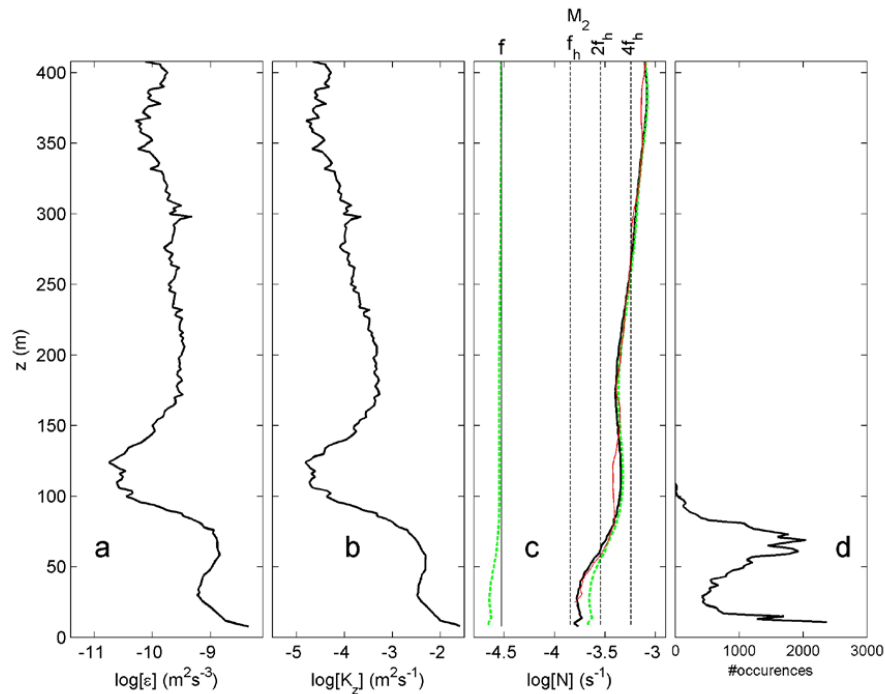
843
844
845
846

Figure 9. As Fig. 3 with identical colour ranges, but for a two-day period with some intense convective turbulence also near the bottom.



847
848
849

Figure 10. As Fig. 4, but associated with Fig. 9 and using different colour ranges.

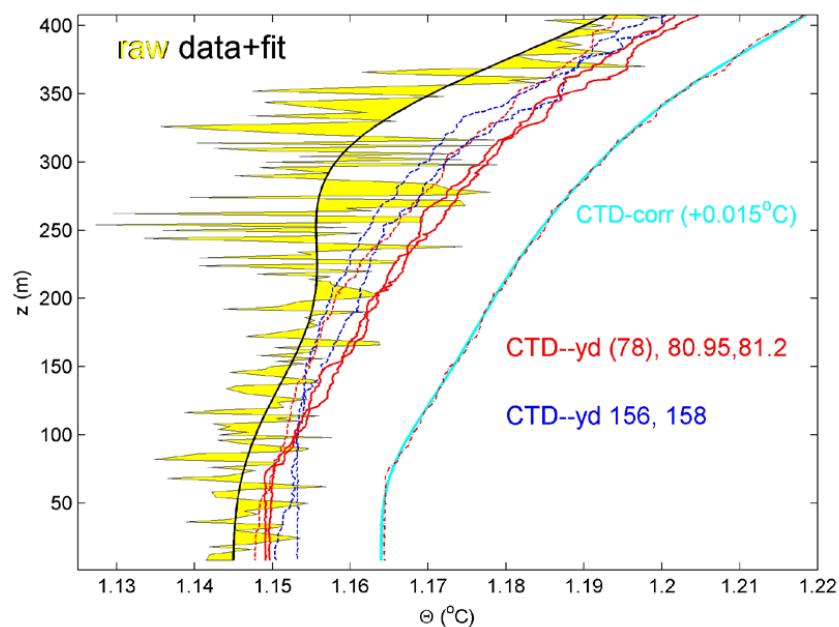


850
 851 **Figure 11.** Profiles of turbulence parameters from entire-record time-averaged
 852 estimates using 1-day drift-corrected, 150 s sub-sampled moored temperature data.
 853 (a) Logarithm of dissipation rate. (b) Logarithm of eddy diffusivity. (c) Logarithm
 854 of small-scale (2 dbar) buoyancy frequency from the T-sensors (black) with for
 855 comparison the mean of the five CTD-profiles smoothed over 50 dbar vertical
 856 intervals from Fig. 2a (red). The green dashed curves indicate the minimum (to the
 857 left of the f -line) and maximum (to the right of the N -profile) inertio-gravity wave
 858 bounds for meridional internal wave propagation (see text). (d) Pdf of the ‘bottom
 859 boundary layer height’, the level of the first passage of threshold $N > 3 \times 10^{-4} \text{ s}^{-1}$
 860 indicating the stratification capping the ‘near-homogeneous’ layer from the bottom
 861 upward. Two peaks are visible, one near 10 mab attributable to bottom friction,
 862 another around 65 mab attributable to internal wave-induced turbulence.
 863



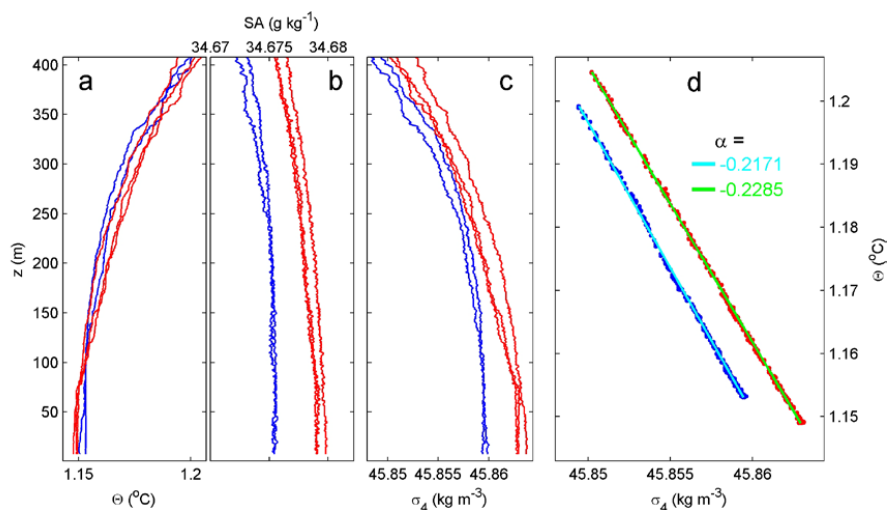
864
865
866
867
868
869

Fig. A1. Photo of thermistor string deployment using the instrumented cable spooling drum onboard R/V Sonne.



870
871
872
873
874
875
876
877
878
879
880

Fig. B1. Conservative Temperature profiles with depth over the lower 400 mab. One-day mean moored sensor data, raw data after calibration (thin black line, yellow-filled) and smooth high-order polynomial fit (thick black solid line). In red are three CTD-profiles within 1 km from the mooring during the first days of deployment (two solid profiles on day 80/81 coincide in time with moored data mean), in blue-dashed are two CTD-profiles after recovery of the mooring. The mean of the two solid red profiles is given by the red/dash-dot profile, 0.015 °C offset for clarity, with its smooth high-order polynomial fit in light-blue to which the moored data are corrected.



881

882

883 **Fig. B2.** Lower 400 m of five CTD-profiles obtained near the T-sensor mooring.

884 Red data are from around the beginning of the moored period, blue from after

885 recovery. (a) Conservative Temperature. (b) Absolute Salinity with x-axis range

886 matching the one in a. in terms of equivalent relative contributions to density

887 variations. The noise level is larger than for temperature. (c) Density anomaly

888 referenced to 4000 dbar. (d) Density anomaly – Conservative Temperature

889 relationship ($\delta\sigma_4 = \alpha\delta\Theta$). The data yielding two representative slopes after linear fit890 are indicated (the mean of 5 profiles gives $\langle\alpha\rangle = -0.223 \pm 0.005 \text{ kg m}^{-3} \text{ } ^\circ\text{C}^{-1}$).

891